ACS APPLIED MATERIALS & INTERFACES

Research Article

www.acsami.org

K-Enriched WO_3 Nanobundles: High Electrical Conductivity and Photocurrent with Controlled Polarity

Zhibin Hu,[†] Zhuan Ji,[‡] Wilson Weicheng Lim,[†] Bablu Mukherjee,[†] Chenggang Zhou,[‡] Eng Soon Tok,[†] and Chorng-Haur Sow*[,†]

[†]Department of Physics, National University of Singapore, 2 Science Drive 3, Singapore 117542, Singapore

[‡]Faculty of Materials Science and Chemistry, China University of Geosciences Wuhan, 388 Lumo Road, Wuhan 430074, China P. R.

ABSTRACT: Potassium ions are successfully intercalated into WO_3 nanobundles with the integrity of the pseudo-orthorhombic structure remaining intact. The nanobundles display a 5-fold increase in the electrical conductivity. It changes from a value of 10^{-4} Sm^{-1} for pure WO_3 to 40 Sm^{-1} upon potassium intercalation. The electrical conductivity also increases by ~200 times as temperature increases from 23 to 200 °C whereby analysis shows a thermal activation energy of ~1 eV. Density functional theory calculations show that K ions cause the reduction of the surrounding W atoms and lead to an increase in the electron population in the conduction band. Hence, the conductivity of the K-WO_3 nanobundles is greatly enhanced. The calculated band structure also shows a gap of 1 eV that is consistent with the measured thermal activation energy. Upon illumination of focused laser beam, individual and isolated nanobundle displays significant photon induced current (9 nA) without external bias at low laser power (2 mW); the amplitude and polarity of photocurrent could be controlled by location of laser spot.

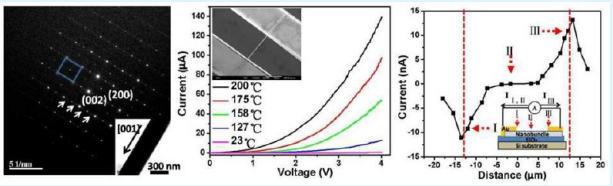

KEYWORDS: *intercalated WO_3, nanobundle, potassium, electric conductivity, photocurrent*

I. INTRODUCTION

The lattice of tungsten oxide is capable of accommodating considerable ion insertion. Modified by ion incorporation, and together with oxygen deficiency commonly found in these compounds, WO_3 displays new properties and exhibits broad technological applications.[1−3] Such applications include electrochromic devices,[4−6] batteries,[7] photochromic devices,[8] gas sensors,[9] and catalysts.[10,11] However, upon the intercalation, the structure of WO_3 is known to deform and proceed to higher symmetry. Intercalation of alkali metal ions into WO_3 by the electrochemical method reveals the phase transition from monoclinic phase to tetragonal phase occurs with $x \sim 0.1$ (Li_xWO_3) and further deforms to cubic phase with $x \sim 0.36$.[12,13] The chemical reduction of WO_3 is also accompanied by structural changes. The lattice tends to eliminate these oxygen vacancies by a crystal shear mechanism, where groups of edge sharing WO_6 octahedra are rearranged along some crystallographic planes.[14−16] Further reduction involving the formation of pentagonal columns occurs when $x > 0.13$ (WO_{3-x}). Schematic images in Figure 1 display the monoclinic structure of WO_3 and the structure of W_5O_{14} in the [001] direction. Clearly, the monoclinic structure of WO_3 deforms after chemical reduction and displays a network of hexagonal and pentagonal columns.[14] To date, intercalating cationic species into WO_3 structure and chemical reduction of WO_3 without giving rise to severe structural deformation or a change of phase has remained a technical challenge.

Recently, we have developed a simple method to synthesize K intercalated MoO_3 single crystalline nanostructure by thermal evaporation on mica substrate.[17] We showed that the layered

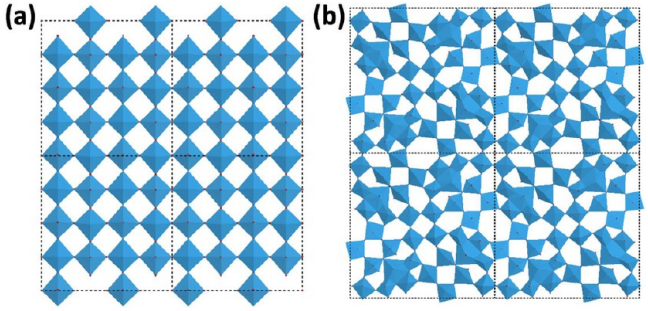

Figure 1. Schematic representation of (a) monoclinic WO_3 in the [001] direction and (b) W_5O_{14} in the [001] direction with a network of hexagonal and pentagonal columns.

MoO_3 structure was found to be preserved despite the large amount of K atoms intercalation. In addition, the electrical conductivity of the K enriched MoO_3 nanomaterial was also enhanced by 7 orders of magnitude. In this paper, the same growth method is used but applied to grow K enriched WO_3 materials. We show that stable K-intercalated WO_3 single crystalline nanostructure with enhanced electrical and optical properties can also be formed. Unlike previous work on intercalated WO_3, this method of growth allows a high amount of K atoms to be intercalated while preserving the pseudo-orthorhombic structure (monoclinic structure with β close to

Received: December 27, 2012
Accepted: April 22, 2013
Published: April 22, 2013

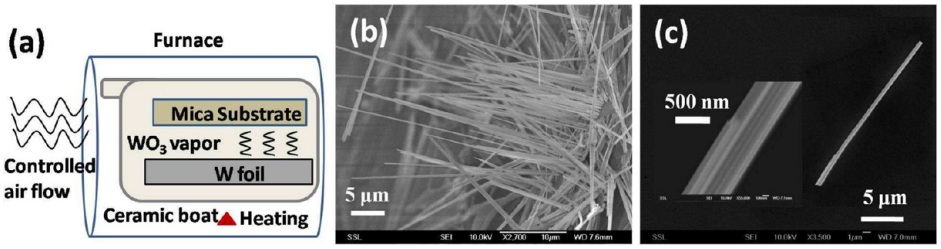

Figure 2. (a) Schematic of the synthesis system. (b) Top view SEM image displays nanobundle grown on the cleavage of mica substrate. (c) Typical morphology of a single K_xWO_3 nanobundle. The inset image is a zoomed in image of the left end of the nanobundle.

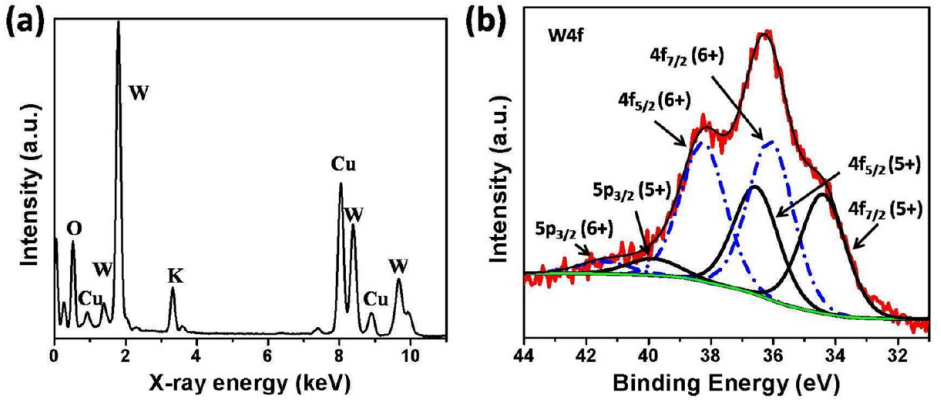

Figure 3. (a) EDS spectrum of an individual nanobundle on TEM grid. (b) XPS spectrum of W4f peaks in the nanobundle. The raw data (red curve) is fitted by W^{6+} peaks (blue dash curve) and W^{5+} peaks (black solid curve).

90°)[12] of WO_3, albeit with lattice expansion along *a*- and *c*-axes and contraction along the *b*-axis. The structure obtained also exhibits substantially high electrical conductivity with the value enhancing five orders from 10^{-4} Sm^{-1} of WO_3 to 40 Sm^{-1} upon potassium intercalation. This value further increases 200 times when temperature increases from 23 to 200 °C. The electrical conductivity is also found to be thermally activated with an energy barrier of ∼1 eV. Density functional theory (DFT) under the generalized gradient approximation (GGA) is utilized to understand the variation of electronic structure of the nanomaterials upon insertion of K ions and to explain the observed high n-type conductivity. Both calculated band structure and measured thermal activation energy consistently suggest that only a small amount of energy is required to excite the localized electrons to the conduction band. As a result, the nanobundle exhibits significant photon induced current (9 nA) without external bias under low laser power (2 mW) while the value measured in reports concerning other semiconductor nanomaterials ranged from ∼10 to ∼500 pA.[18−20]

II. EXPERIMENTAL SECTION

K_xWO_3 nanostructures are synthesized by the thermal evaporation method in a horizontal tube furnace. The synthetic scheme used in the present study is shown in Figure 2a. A W foil (5 mm × 5 mm × 0.05 mm in size, from Aldrich Chemical Co., Inc., purity 99.99%) is used as the W source and placed in ceramic boat and a muscovite mica sheet ($K_2O{\cdot}3Al_2O_3{\cdot}6SiO_2{\cdot}2H_2O$, 8 mm × 8 mm in size, from Alfa Aesar Co., Inc.) is placed on top of the W foil as substrate and K source. The ceramic boat containing W foil and mica sheet is inserted into the furnace (Carbolite MTF 12/25/250) and placed at the center of the heating zone of the furnace. The system is heated for 3 days in ambient at 650 °C, and a fan is used to blow fresh air into the furnace to provide enough oxygen for the growth.

The morphology, structures, and chemical composition of the as-synthesized individual nanostructures are characterized by using field emission scanning electron microscopy (FESEM, JEOL JSM-6700F), transmission electron microscopy (TEM, JEOL JEM-2010F, 200 kV), and energy-dispersive X-ray spectrometers (EDS) equipped in the TEM. X-ray diffraction (X'PERT MPD, Cu Kα (1.5418 Å) radiation) measurement and X-ray photoelectron spectroscopy (XPS, Omicron EA125 analyzer, monochromatic Mg Kα source (1253.6 eV)) measurement are performed on the substrate with a large area of as-synthesized nanostructures to measure the averaged lattice structure of material and to determine the averaged chemical composition in the synthesized product.

For electrical property measurement, the single nanobundle device is fabricated by transferring individual nanobundle from the growth substrate to SiO_2/Si substrate and utilizing the photolithography method to achieve designed metal (Au(400 nm)/Cr(10 nm)) finger electrodes (of gap ∼15 μm) that make contact with the nanobundle. The electrical measurements are carried out using a Keithley 6430 source-measure unit. For photocurrent measurements, the linearly polarized diode laser beam (λ = 532 nm SUWTECH, LDC-2500) is directed into the microscope via mirrors. Inside the microscope, the laser beam is reflected by a beam splitter toward a 100× objective lens. The objective lens focuses the laser beam onto the device that is positioned on the translation stage. The focused laser beam with spot size around 2 μm and power of 2 mW is locally directed on the sample.

III. RESULTS AND DISCUSSION

K_xWO_3 nanobundles are synthesized by the thermal evaporation method. The deposition of the oxidized W yields nanobundles on the cleavage of mica substrate, including the edge of the substrate and steps on the top surface. Figure 2b displays the top view SEM image of the edge of the mica substrate. These nanobundles extend out of cleavage with a length of 20−70 μm, a width of 500−700 nm, and a thickness of 150−300 nm. For further observation, individual nanobundle is transferred to Si substrate. Since the nanobundles are firmly attached to the substrate, only a segment of the nanobundle is

transferred to Si substrate as shown in Figure 2c with the length, width, and thickness of 21 μm, 550 nm, and 250 nm, respectively. The inset displays the enlarged image of the left end of the nanobundle, indicating that the nanobundle is constructed by several parallel nanobelts. These nanobelts are much thinner with a width and a thickness of approximately 100 and 80 nm.

These nanobundles are transferred to a TEM grid for further analysis. Figure 3a shows the EDS spectrum elemental analysis for an individual nanobundle in TEM. The Cu peaks come from the TEM grid while the K, W, and O peaks originate from the nanobundle. It reveals that tungsten oxide nanobundle contains a significant percentage of K atoms (denoted as K_xWO_3). The measurement is repeated on different locations in the same nanobundle and on different nanobundles as well. The results show that the K/W ratio in every K_xWO_3 nanobundle is uniform in the same nanobundle but differs between different nanobundles with x ranging from 0.18 to 0.28. To further identify the oxidation state of the W ions in the material, the XPS experiment is performed to measure the average oxidation state of W atoms in nanobundles on mica substrate. The energy distribution of W 4f photoelectrons is shown in Figure 3b. The original data (red curve) is fitted by W^{6+} peaks (blue dash curve) and W^{5+} peaks (black solid curve). The peaks at 36.1, 38.2, and 42.0 eV represent emission from W $4f_{7/2}$, $4f_{5/2}$, and $5p_{3/2}$ levels from the W atoms in the 6+ oxidation state while the peaks at 34.4, 36.6, and 40.2 eV come from W $4f_{7/2}$, $4f_{5/2}$, and $5p_{3/2}$ levels from the W atoms in the 5+ oxidation state.[16] The area ratio of W^{6+} over W^{5+} is around 4:3, revealing the valency of W is +5.57. The most common K/W atomic percentage ratio found in individual nanobundles is ~0.23, and the combined valency of K and W is +5.80 in the material. Considering the neutrality of the nanobundle, the stoichimetry of O is around 2.9, implying the existence of oxygen vacancies in the structure of WO_3.

To characterize the structure of the complex, the selected area electron diffraction (SAED) pattern of the K_xWO_3 nanobundles on the (010) surface is shown in Figure 4a with the inset image displaying a low-magnification TEM image of the nanobundle along the [001] growth direction. The nanobundle exhibits a pseudorectangular diffraction pattern with $\beta = 90.37 \pm 0.02°$ along the [010] zone axis highlighted by a blue rectangle formed by large bright spots. It represents the WO_3 structure adopting a pseudo-orthorhombic configuration.

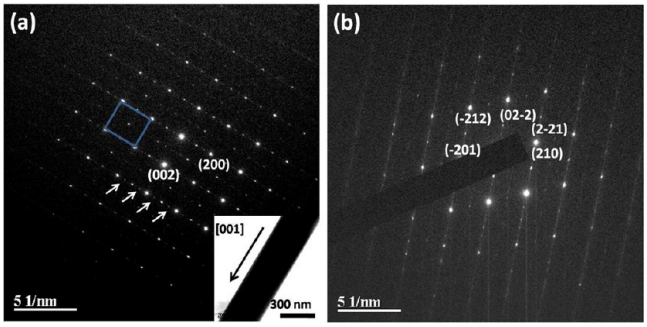

Figure 4. (a) Electron diffraction pattern of the K_xWO_3 nanobundle along the [010] zone axis; the highlighted blue rectangle formed by large bright spots represents the lattice structure of the K intercalated WO_3. The inset image shows a TEM image of the typical K_xWO_3 nanobundle growing in the [001] direction. (b) Electron diffraction pattern of the nanobundle along the [122] zone axis.

Between every two bright spots, there is one weaker spot located in the middle along the [100] direction of the K_xWO_3 nanobundle indicated by white arrows. These smaller diffraction spots suggest that K_xWO_3 nanobundles possess a periodic superstructure with two primitive cells along the [100] direction. Since the diffraction pattern along the [010] zone axis only provides the structure information along *a*- and *c*-axes, the diffraction pattern along the other zone axis is also captured to achieve lattice information along the *b*-axis. Figure 4b shows the SAED pattern of the nanobundle along the [122] zone axis; the diffraction pattern is similar with the projection of pseudo-orthorhombic structure along the [122] zone axis. With the help of both diffraction patterns, lattice constants of each individual nanobundle can be derived. Upon the considerable uptake of K atoms in the WO_3 structure, the pseudo-orthorhombic structure is preserved with the expansion of *a*- and *c*-axes and contraction of the *b*-axis as shown in Table 1. As

Table 1. Measured Lattice Constants of the WO_3 Powder and the K_xWO_3 Nanobundle

		a (Å)	*b* (Å)	*c* (Å)
WO_3	exp.	7.40	7.60	7.79
	rep.[16]	7.39	7.57	7.79
K_xWO_3	$X = 0.18$[a],a	7.44	7.45	7.79
	average[b],a	7.58	7.32	7.81
	$X = 0.28$[c],a	7.63	7.15	7.83

[a]The data in [a] and [c] is calculated from TEM diffraction pattern; the data in [b] is calculated from XRD peaks with *x* around 0.23.

the K content in the lattice increases, the atomic percentage ratio of K over W increases from 0.18 to 0.28, the lattice constant *a* increases from 7.44 to 7.63 Å while *c*-axis expands a bit from 7.79 to 7.83 Å as shown in Figure 5a,b respectively. The transferred nanobundles are easily placed on the TEM grid with [010] direction perpendicular to the grid; it is hard to tilt the nanobundle to the suitable angle to achieve the same diffraction pattern that contains information along the [010] direction for all nanobundles. Thus, the lattice constant *b* at various K concentrations is not systematically studied.

The growth of K_xWO_3 nanobundle appears to occur when evaporated oxidized tungsten vapor reacts with the cleavage surface of mica to form K_xWO_3 complex. With the continuous adsorption of WO_3 vapor and K ions from mica substrate, K_xWO_3 becomes oversaturated on the cleavage surface and K_xWO_3 nanobundle nucleates out of the surface in the preferred direction, similar to the growth of K_xMoO_3 nanobundle.[17] According to the described growth mechanism, the structure of K_xWO_3 would be related to the initial WO_3 powder where the oxidized tungsten vapor comes from. During the synthesis, the W foil was gradually oxidized and turned into yellow-green WO_3 powders. The structure of these yellow-green WO_3 powders suggests the structure of K_xWO_3 with $x = 0$. The X-ray diffraction was utilized to identify the structure of powder. Upper curve of Figure 6 shows the powder exhibits orthorhombic structure of WO_3 with lattice constant $a = 7.40$ Å, $b = 7.60$ Å, and $c = 7.79$ Å; the values are consistent with the reported result.[21] These values contribute to the first data point in Figure 5, which display the lattice constant of K_xWO_3 without K insertion. The red exponential fitted curves display that both lattice constant *a* and *c* expand exponentially with more K ions inserted but to a different degree. It is noted that, upon significant amount of K insertion ($x = 0.28$), the

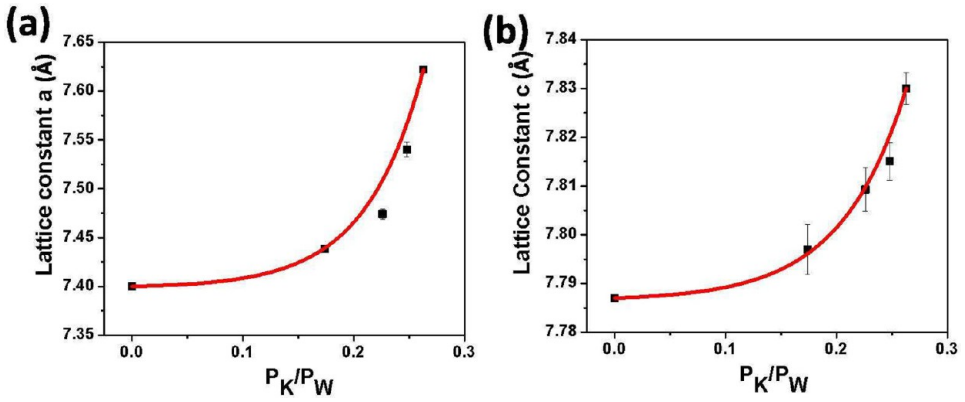

Figure 5. Lattice constant (a) *a* and (b) *c* at various atomic percentage ratio of K over W. The red curves are exponential fitting curves of data points.

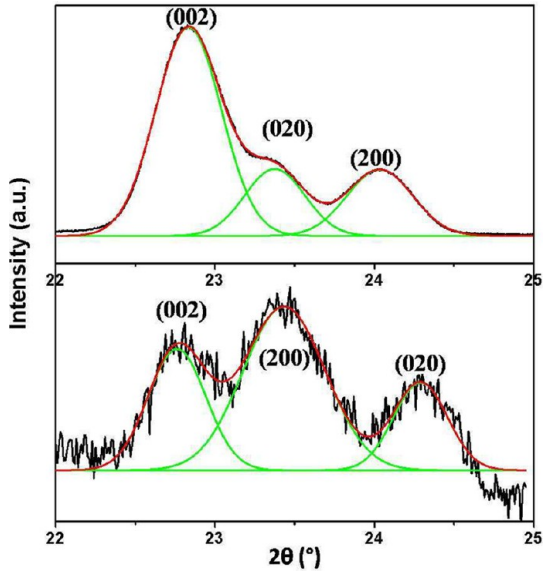

Figure 6. XRD spectrum of WO_3 powder (upper curve) and K_xWO_3 nanobundles (lower curve).

nanobundle maintains a well aligned pseudo-orthorhombic single crystalline structure as displayed by SAED patterns.

The K_xWO_3 nanobundles are also studied by XRD, and the lower curve in Figure 6 shows the structure of nanobundles. According to the structure of WO_3, these three peaks denote the (200), (020), and (002) surfaces. From peak position, lattice constants of 7.81, 7.58, and 7.32 Å are calculated corresponding to the peaks from left to right. Since the averaged K/W atomic percentage ratio measured by large scale EDS measurement is ∼0.23 and the trends shown in Figure 4 suggest the averaged lattice constant should lie between the maximum and minimum value, three peaks are identified as (002), (200), and (020), respectively, and the lattice constants determined are listed in Table 1. The significant peaks confirm the pseudo-orthorhombic structure of the nanobundle analyzed above. Compared with the fitting curve in Figure 5, both values of lattice constant *a* and *c* in the curve denoting the atomic percentage ratio of K over W are around 0.23, which is consistent with the measurement by EDS.

According to previously reported formation of intercalated WO_3 and reduced WO_3, phase transition is observed to occur upon intercalation or chemical reduction. In these reported works, the monoclinic structure of WO_3 upon intercalation proceeds to higher symmetry. In Li_xWO_3 for example, this occurs initially by a phase transition to a tetragonal phase with $x \sim 0.1$ and later by phase transition to a cubic phase when $x \sim 0.36$.[12,13] Upon chemical reduction, the structure of WO_3 changes by crystal shear mechanism, where groups of edge sharing WO_6 octahedra are rearranged along some crystallographic planes.[14−16] In the case of tungsten oxide with similar stoichiometry $W_{20}O_{58}$, WO_6 octahedras are rearranged with crystal shear planes along the (103) direction and the unit cell (monoclinic) is enlarged with a = 12.1 Å, b = 3.78 Å, and c = 23.4 Å.[22] These phase transitions are however not observed in

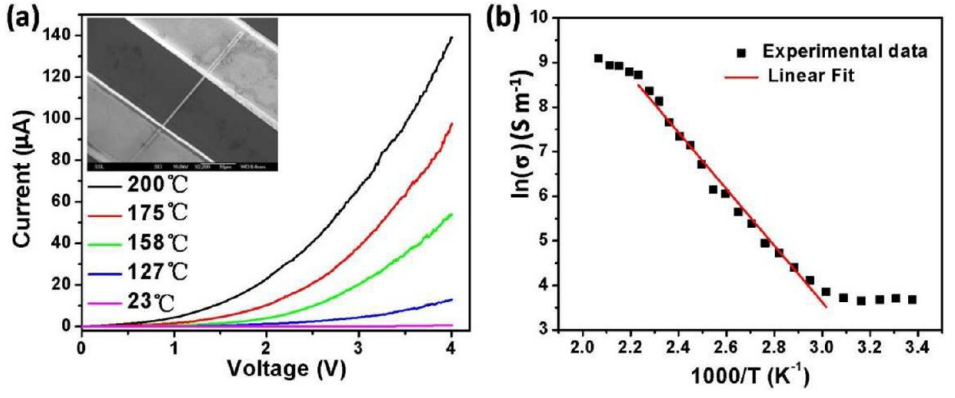

Figure 7. (a) *I*−*V* curve of individual K_xWO_3 nanobundle under different temperatures. Inset figure shows SEM image of an individual nanobundle contacted by electrodes. (b) Temperature dependence conductivity of the nanobundle in log scale at voltage of 4 V.

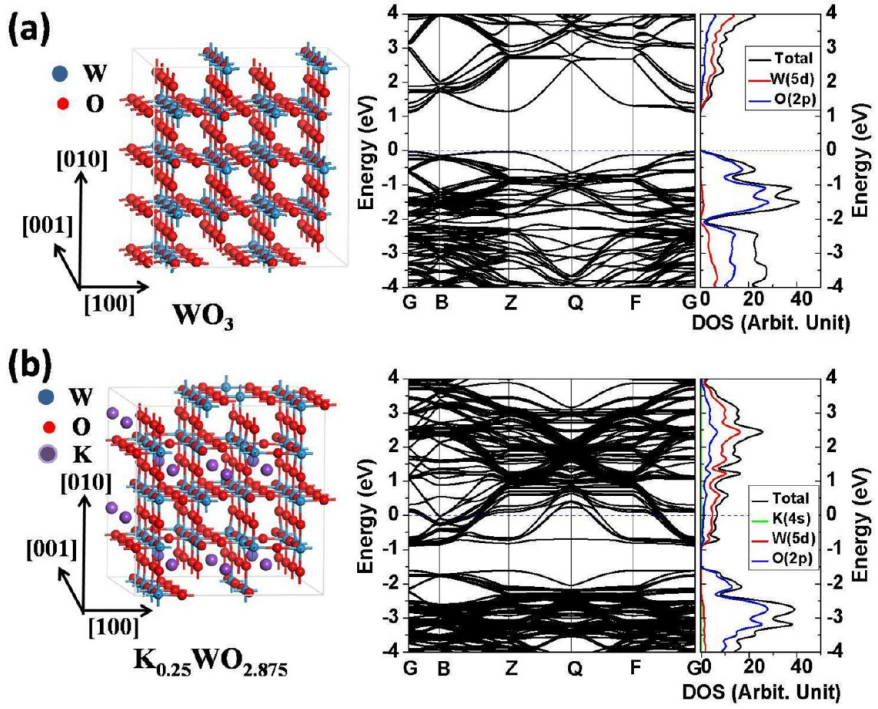

Figure 8. Atomic structure, calculated band structure, and the density of states (DOS) of (a) WO_3 and (b) $K_{0.25}WO_{2.875}$.

our K_xWO_3 nanobundles; the pseudo-orthorhombic structure is preserved even with the intercalation of a great amount of K atoms and chemical reduction of WO_3.

We next fabricate an individual nanobundle device by the method described in the Experimental Section. The inset image in Figure 7a displays the SEM image of an individual K_xWO_3 nanobundle contacted by electrodes. The electrical measurements are carried out using a Keithley 6430 source-measurement unit. As a comparison, as-grown WO_3 powder is compressed and deposited on a similar electrode pattern on SiO_2/Si substrate; the measured current is on the order of ca. 100 nA at ca. 4 V. From the effective length of electrode, separation between electrodes, and thickness of the powder, we estimated the electric conductivity of the WO_3 powder to be 10^{-4} S m^{-1}, consistent with the reported value of WO_3 film.[23] For the K_xWO_3 nanobundle, at room temperature, the measured current is 0.7 μA at a bias of 4 V. From the measured effective length and cross section of the nanobundle, the electrical conductivity is estimated to be 40 S m^{-1}. It is remarkable that the electrical conductivity is enhanced substantially by 5 orders of magnitude from 10^{-4} S m^{-1} of the WO_3 powder to 40 S m^{-1}. The $I-V$ curve displays typical semiconductor behavior, and further field-effect transistor (FET) measurement shows that the K_xWO_3 nanobundles exhibit n-type semiconductor behavior. The conductivity of the K_xWO_3 nanobundles increases rapidly upon heating as shown in Figure 7a. At the bias of 4 V, the current increases from 0.7 to 140 μA as the temperature increases from 23 to 200 °C, raising the conductivity by 200 times from 40 to 8000 S m^{-1}.

Subsequently, the conductivity as a function of reciprocal of temperature is plotted on a log scale as shown in Figure 7b. Two kinks in the curve are clearly observed at 331 and 448 K. At the temperature below 331 K, conductivity does not change significantly. As temperature increases from 331 to 448 K, the log scale of conductivity varies linearly with reciprocal of temperature. In this region, electron conductivity increases exponentially with reciprocal of temperature. According to $\sigma = ne\mu$, where σ is the conductivity of nanobundle, μ is the mobility of electrons, and n is the electron density, the mobility in the region does not vary significantly due to relatively low electron density. The electron conductivity is thus determined by electron density, and the variation of σ with temperature in this linear range can be attributed to change of electron density with temperature. Based on the thermally activated transport model,[24,25] $\ln(n) = \ln(n_0) - W/2kT$, where n is the electron density, n_0 is the density value when T is infinity, k is the Boltzmann constant, and W is the thermal activation energy. The thermal activation energy is determined to be around 1 eV based on the slope of a linear fit to the data (Figure 7b), suggesting this energy is required to thermally excite localized electrons to the conduction band. The effect of phonon scattering increases for thermally excited lattice atoms, and the effect becomes more prominent at high temperature due to sufficient high electron density. Consequently, above 448 K, the slope of conductivity decreases due to the decreasing mobility induced by significant phonon scattering.

To interpret the experimental results, we perform density functional theory calculations to understand the structural and electronic properties of the pure and K-intercalated WO_3 materials. Since the thicknesses and widths of the WO_3 powders and the K_xWO_3 nanobundles are several orders of magnitude larger than the size of atoms, we employ a 3-dimensional periodic bulk-like structure to model the present system. A 2 × 1 × 1 supercell of the pseudo-orthorhombic WO_3 primitive lattice containing 16 W atoms and 48 O atoms (Figure 8a) is first selected to model the pure WO_3 powder. The fully optimized lattice of the WO_3 supercell, with the lattice constants a = 7.45 Å, b = 7.65 Å, and c = 7.76 Å, is in agreement with the experimental data shown above and the reported XRD data,[21] suggesting that our computational method is reliable for predicting structural information of the materials we deal with. On the basis of the stoichiometry of the

dx.doi.org/10.1021/am303253p | ACS Appl. Mater. Interfaces 2013, 5, 4731−4738

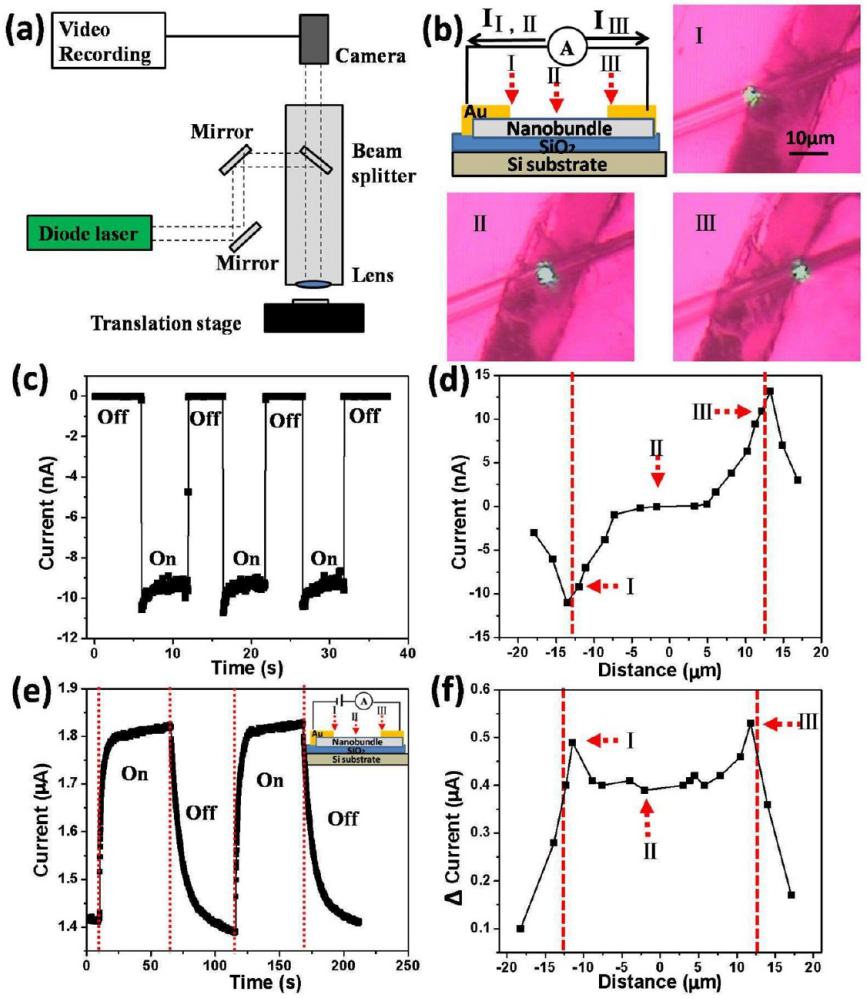

Figure 9. (a) Schematic of photon response measurement setup with focused laser beam irradiation on K_xWO_3 nanobundle. (b) Schematic of focused laser beam locally irradiating at three different locations and three optical images showing the position of laser spot on nanobundle device. (c) Photon induced current measured when laser spot was directed at location I without externally applied bias voltage. (d) Photon induced current at different distances between the center of the laser spot and the center of the nanobundle at zero bias. Two red broken lines denote the edge of electrode. (e) Photocurrent measured under external bias voltage of 4 V with laser spot directed at location II on the nanobundle device. Inset shows schematic of focused laser beam locally irradiating at three different locations under external bias. (f) The photon enhanced current at different distances between the center of laser spot and the center of nanobundle under external bias voltage of 4 V.

nanobundle, we substitute two O atoms with K atoms and place two K atoms as intercalants in the supercell. The optimized structure of $K_{0.25}WO_{2.875}$ in Figure 8b shows that, either as intercalants or occupants, K atoms finally relocate to the tunnel along the [001] direction of the cell, where each K atom is encapsulated by 3 or 4 adjacent O atoms. The oxygen vacancies lead to slight distortion of the lattice, while the inserted K atoms cause an expansion of 0.2 Å along the *a*-axis, which is in good agreement with experimental observation.

The electronic structures of pseudo-orthorhombic WO_3 and K_xWO_3 are calculated on the basis of the optimized structure. The band structure and density of states of WO_3 are displayed in Figure 8a. The valence band is largely dominated by the 2p orbitals of oxygen, while the conduction band consists of chiefly the 5d states of tungsten with a significant contribution from the 2p states of oxygen. This calculated band structure of pseudo-orthorhombic WO_3 with a direct band gap of ∼1.2 eV is consistent with other reports.[26,27] The band structure of the $K_{0.25}WO_{2.875}$ lattice is depicted in Figure 8b. Upon potassium uptake in the lattice, the electronic structure undergoes a substantial change due to the charge transfer from potassium to tungsten, which forces electrons to populate the conduction band. The projected density of states (PDOS) for the K-4s and W-5d states indicate that K atoms are fully ionized and the adjacent W atoms are accordingly reduced, which is consistent with the observation from XPS measurement. Because of the strong overlap between the W-5d orbitals and the O-2p orbitals in the conduction band, the transferred electrons are abundant in number and readily delocalize; thus, the electrical conductivity is significantly enhanced.

In the projected density of state of $K_{0.25}WO_{2.875}$ in Figure 8b, the Fermi level (at 0 eV) is located in the conduction band and these electrons can easily be excited and delocalized to the higher energy states directly above upon heating, as there are continuous available states in the conduction band (no gap). The excitation of these electrons to these states leaves unoccupied states, especially the ones near the bottom of conduction band. According to the band structure in Figure 8b, the minimum enegy to excite the valence electrons to the conduction band can be given by CBM−VBM and it has a value of ∼1 eV. Thus, the electrons in the valence band require at least ∼1 eV to be excited to these unoccupied states in the

dx.doi.org/10.1021/am303253p | ACS Appl. Mater. Interfaces 2013, 5, 4731−4738

conduction band to contribute to the measured current. Consequently, at relatively low temperature due to the insufficient thermal energy provided, electrons in the valence band could not be excited to the conduction band to increase the current density. As a result, below 331 K, the conductivity does not change with temperature as shown in Figure 7b. When sufficient energy is provided, the localized electrons in the valence band can be excited to the unoccupied states in the conduction band and contribute to the conductivity. As such, the electrical conductivity is greatly enhanced above 331 K. Notably, the gap of ∼1 eV is close to the thermal activation energy for electrical conductivity shown in Figure 7b.

The small activation energy of the material (∼1 eV) implies the nanobundle is a viable candidate for the investigation of opto-electric response. Upon laser illumination, localized electrons in the nanobundle can be excited by photons and contribute to the current. Figure 9a shows the schematic of the photon response measurement setup with focused laser beam irradiation on the K_xWO_3 nanobundle. Details of the laser arrangement are described in the Experimental Section. Focused laser beam with spot size around 2 μm and power of 2 mW is locally directed at specific locations as shown in Figure 9b. In location I and III, laser is focused on the left and right electrode-nanobundle junction, respectively. In location II, the spot lands on the middle of the nanobundle.

Figure 9c displays the measured current between electrodes when the laser is directed at location I without externally applied bias voltage. In the absence of laser beam irradiation, there was no current detected. The moment the laser is present, current increases to −9 nA within 50 ms. The current returns to 0 again when the laser is blocked. It is noted that the photon induced current in the material is quite significant compared with other semiconductor nanomaterial with typical values ranging from ∼10 to ∼500 pA under similar laser power.[18−20] Focused laser beam is directed at different locations, and the corresponding photon induced current is measured as shown in Figure 9d. The distance indicated in the horizontal axis is measured with respect to the center of the nanobundle, and the two broken lines denote the edge of electrodes. Here, we observe surprising photocurremt results at zero external bias. The photocurrent response exhibits an opposite polarity when the laser beam is focused at two different ends of the nanobundle-metal junction. Negligible photocurrent is observed when the focused laser beam is directed at the middle of the nanobundle.

The observed properties of the photocurrent can be interpreted by considering the nanobundle-gold system as a back-to-back Schottky diode model. Observations made in Figure 9d can be attributed to the properties of the Schottky barrier formed at the nanobundle-gold contacts. Shining of the laser may facilitate an increase in the photogenerated electrons to travel from nanobundles to the gold contact and give rise to the photocurrent. When the laser is shone onto the other contact, a similar process occurs but the polarity of the photocurrent is reversed. When the laser is shone on the middle of the nanobundle, the charge carriers do not have sufficient energy to diffuse across the nanobundle and many are lost through recombination and scattering. Thus, the photocurrent with laser shining on the middle of the nanobundle is found to be negligible. A similar observation is made in the case of Nb_2O_5 nanowires.[18] In addition, the localized thermal heating caused by the focused laser can give rise to a thermoelectric effect at the nanobundle-gold interface. This effect can give rise to net diffusion of electrons from the nanobundle to the gold electrode at the junction. Similarly, shining the laser on a different junction can control the polarity of the photocurrent.

When external bias voltage is applied, under laser illumination, localized electrons are excited by photons and enhance the current; the setup is shown in the inset image in Figure 9e. The curve in Figure 9e displays the measured current between electrodes when the laser is shone at location II with an external applied bias voltage of 4 V. When the laser is blocked, current is around 1.42 μA. The moment the laser is on, current increases to 1.82 μA in 12 s. The current drops to 1.42 μA again when the laser is off. The current increases rapidly at the beginning (0.2 μA in the first second) denoting that part of the excited electrons originated from photon excitation and the current further increases slowly (0.2 μA in the following 10 s) suggesting that part of the excited electrons originated from the thermal effect.[18] Focused laser is directed at different locations as shown in the inset of Figure 9e; the distance is measured with respect to the center of the nanobundle, and the corresponding photon enhanced current under external bias voltage of 4 V is detected as shown in Figure 9f. In the curve, the two highest amplitudes take place when the laser spot is shone on the electrode-nanobundle junction (location I and III) and the amplitude gradually decreases a bit and is finally maintained (location II) as the laser spot moves to the center of nanobundle.

As shown in Figure 9f, when the laser spot is directed at location II, the current is enhanced by 0.4 μA, which suggests that a significant amount of electrons are excited by the focused laser beam. As discussed above, low energy is required for localized electrons to be excited to the conduction band and contribute to the current. The difference between zero applied bias and nonzero applied bias is that, with applied bias, the additional charge carriers can be readily driven across the nanobundle and this gives rise to increased current. Regardless of where the laser is focused on the nanobundle, the photogenerated charge carriers will be driven along the nanobundle in the same direction. As a result, the polarity and amplitudes of enhanced current are similar as the laser spot moves from left to right in Figure 9f. Moreover, it should also be noted that the magnitude of the photocurrent with applied bias is much higher than the photocurrent obtained under zero bias.

IV. CONCLUSIONS

In summary, we have presented a simple but effective technique to grow K intercalated WO_3 nanobundles with the pseudo-orthorhombic structure remaining essentially intact. The nanobundles adopt a bottom-up growth model via thermal evaporation to intercalate K atoms into the WO_3 lattice. Using a device comprising a single nanobundle, we measure the $I-V$ curves of the K_xWO_3 nanobundle. It is found that the material displays substantially higher electrical conductivity and the conductivity further increases by 200 times at elevated temperature. Density functional theory is used to elucidate the structureof the K_xWO_3 and to understand the origin of the high conductivity behavior of the material. The calculated band structure of the $K_{0.25}WO_{2.875}$ indicates the K atoms are fully ionized, giving rise to the reduction of the adjacent W atoms, which is consistent with the observation from XPS measurement. As a consequence, the conduction band is populated, leading to electron delocalization and high conductivity of the

nanobundle. On the basis of the calculated band structure, these delocalized electrons are easily excited to available states above and leave the states unoccupied, thus making these states available to electrons in the valence band at ~1 eV below. The value is consistent with the measured thermal activation energy of the nanobundle, and the mechanism explains the significant enhancement of electrical conductivity upon heating (increases 200 times from 23 to 200 °C). Under focused laser illumination, the nanobundle displays significant photon induced current (9 nA) without external bias at low laser power (2 mW), and the amplitude and polarity of photocurrent can be controlled by location of the laser spot. The novel properties of the K-enriched WO_3 nanobundles are envisaged to significantly enhance the performance of the electronic devices using compounds in the metal-intercalated WO_3 family, and the simple preparation method opens a new opportunity to develop nanostructured materials of large-ion intercalated metal oxides.

AUTHOR INFORMATION

Corresponding Author

*E-mail: physowch@nus.edu.sg.

Notes

The authors declare no competing financial interest.

ACKNOWLEDGMENTS

The authors acknowledge the support of National University of Singapore FRC Grant (HC: R-144-000-281-112). The computational work was implemented on the HPC center of China University of Geosciences Wuhan. Z.J. and C.Z. acknowledge the support of the National Natural Science Foundation of China (Grant 20973159) and the Fundamental Research Funds for the Central Universities, China University of Geosciences Wuhan (Grant CUG120115).

REFERENCES

(1) Hjelm, A.; Granqvist, C. G.; Wills, J. M. *Phys. Rev. B* **1996**, *54*, 2436−2445.
(2) Srinivasan, A.; Miyauchi, M. *J. Phys. Chem. C* **2012**, *116*, 15421.
(3) Amano, F.; Tian, M.; Wu, G.; Ohtani, B.; Chen, A. *ACS Appl. Mater. Interfaces* **2011**, *3*, 4047.
(4) Granqvist, C. G. *Sol. Energy Mater. Sol. Cells* **2000**, *60*, 201−262.
(5) Costa, C.; Pinheiro, C.; Henriques, I.; Laia, C. A. T. *ACS Appl. Mater. Interfaces* **2012**, *4*, 1330.
(6) Karakurt, I.; Boneberg, J.; Leiderer, P. *Appl. Phys. A: Mater.* **2006**, *83*, 1−3.
(7) Yoon, S.; Jo, C.; Noh, S. Y.; Lee, C. W.; Song, J. H.; Lee, J. *Phys. Chem. Chem. Phys.* **2011**, *13*, 11060−11066.
(8) He, T.; M., Y.; Cao, Y.-a.; Yang, W.-s.; Yao, J.-n. *Phys. Chem. Chem. Phys.* **2002**, *4*, 1637−1639.
(9) Aguir, K.; Lemire, C.; Lollman, D. B. B. *Sens. Actuators, B* **2002**, *84*, 1−5.
(10) Chen, X.; Zhou, Y.; Liu, Q.; Li, Z.; Liu, J.; Zou, Z. *ACS Appl. Mater. Interfaces* **2012**, *4*, 3372.
(11) Jiao, Z.; Wang, J.; Ke, L.; Sun, X. W.; Demir, H. V. *ACS Appl. Mater. Interfaces* **2011**, *3*, 229.
(12) Zhong, Q.; Dahn, J. R.; Colbow, K. *Phys. Rev. B* **1992**, *46*, 2554−2560.
(13) Mattsson, M. S. *Phys. Rev. B* **1998**, *58*, 11015−11022.
(14) Frey, G. L.; Rothschild, A.; Sloan, J.; Rosentsveig, R.; Popovitz-Biro, R.; Tenne, R. *J. Solid State Chem.* **2001**, *162*, 300−314.
(15) Polaczek, A.; Pekata, M.; Obuszko, Z. *J. Phys.: Condens. Matter* **1994**, *6*, 7909−7919.
(16) Remškar, M.; Kovac, J.; Viršek, M.; Mrak, M.; Jesih, A.; Seabaugh, A. *Adv. Funct. Mater.* **2007**, *17*, 1974−1978.
(17) Hu, Z.; Zhou, C.; Zheng, M.; Lu, J.; Varghese, B.; Cheng, H.; Sow, C.-H. *J. Phys. Chem. C* **2012**, *116*, 3962−2967.
(18) Tamang, R.; Varghese, B.; Mhaisalkar, S. G.; Tok, E. S.; Sow, C. H. *Nanotechnology* **2011**, *22*, 115202.
(19) Varghese, B.; Tamang, R.; Tok, E. S.; Mhaisalkar, S. G.; Sow, C. H. *J. Phys. Chem. C* **2010**, *114*, 15149−15156.
(20) Liao, Z. M.; Xu, J.; Zhang, J. M.; Yu, D. P. *Appl. Phys. Lett.* **2008**, *93*, 023111.
(21) JCPDS (card No. 89-4480) - International Centre for Diffraction Data 2002.
(22) Chen, J.; Lu, D.; Zhang, W.; Xie, F.; Zhou, J.; Gong, L.; Liu, X.; Deng, S.; Xu, N. *J. Phys. D: Appl. Phys.* **2008**, *41*, 115305.
(23) Gilleta, M.; Aguir, K.; Lemire, C.; Gillet, E.; Schierbaum, K. *Thin Solid Films* **2004**, *467*, 239−246.
(24) Sze, S. M.; Ng, K. K. *Physics of Semiconductor Device*, 3rd ed.; Wiley: New York, 2007; pp 21−25.
(25) Sun, K.-W.; Fan, T.-Y. *Mater. Sci. Appl.* **2010**, *1*, 8−12.
(26) De Wijs, G. A.; de Boer, P. K.; de Groot, R. A. *Phys. Rev. B* **1999**, *59*, 2684−2693.
(27) Chatten, R.; Chadwick, A. V.; Rougier, A.; Lindan, P. J. D. *J. Phys. Chem. B* **2005**, *109*, 3146−3156.